ADVANCED MATERIALS
www.advmat.de

4D Multimaterial Printing of Soft Actuators with Spatial and Temporal Control

*Kun Zhou, Rujie Sun, Jonathan P. Wojciechowski, Richard Wang, Jonathan Yeow, Yuyang Zuo, Xin Song, Chunliang Wang, Yue Shao, and Molly M. Stevens**

Soft actuators (SAs) are devices which can interact with delicate objects in a manner not achievable with traditional robotics. While it is possible to design a SA whose actuation is triggered via an external stimulus, the use of a single stimulus creates challenges in the spatial and temporal control of the actuation. Herein, a 4D printed multimaterial soft actuator design (MMSA) whose actuation is only initiated by a combination of triggers (i.e., pH and temperature) is presented. Using 3D printing, a multilayered soft actuator with a hydrophilic pH-sensitive layer, and a hydrophobic magnetic and temperature-responsive shape-memory polymer layer, is designed. The hydrogel responds to environmental pH conditions by swelling or shrinking, while the shape-memory polymer can resist the shape deformation of the hydrogel until triggered by temperature or light. The combination of these stimuli-responsive layers allows for a high level of spatiotemporal control of the actuation. The utility of the 4D MMSA is demonstrated via a series of cargo capture and release experiments, validating its ability to demonstrate active spatiotemporal control. The MMSA concept provides a promising research direction to develop multifunctional soft devices with potential applications in biomedical engineering and environmental engineering.

1. Introduction

Soft actuators have shown great advantages when interacting with delicate objects, due to their compliance and flexibility,[1] overcoming challenges encountered by traditional robotics. This has enabled applications where precise and controlled manipulation of soft and fragile objects is required, such as in manufacturing and biomedical engineering.[2] The design of a soft actuator typically requires a stimuli responsive material to trigger the actuation. As a result, various stimuli-responsive materials have been demonstrated which interact with magnetic,[3] chemical,[4] or thermal stimuli.[5] Another important parameter is control over the geometrical shape of the actuator which defines the deformation.[6] For example, an isotropic shape, like a sphere can expand or contract its volume, but not achieve bending or twisting deformations, whereas, in comparison, an anisotropic rectangular shape can. The anisotropy of the soft actuator extends to a variety of geometric parameters including the length-width ratio,[7] relative thickness,[8] and porosity.[4c] It is therefore important to define both the stimulus which initiates the actuation, and the resulting geometry of the soft actuator.

Among the vast array of soft actuator fabrication methods, 3D printing enables flexibility in the design of a soft actuator and imparts convenience,[9] cost-efficiency,[9a,10] and reproducibility,[11] making it an ideal method for soft actuator fabrication. As an extension, 4D printing, where 3D printed materials are designed with the capability to transform their shapes in response to stimuli,[12] lends itself as an integrated method to fabricate soft actuators.[13] One limitation of producing soft actuators by 4D printing is ensuring material compatibility of the stimuli responsive material with the printing process. Considering stereolithography based 3D printing techniques, due to their higher resolution compared with extrusion-based methods, a photoreactive monomer or polymer with low viscosity is required. Among the available materials, stimuli-responsive hydrogels[4c,14] are widely used due to their controllable swelling ratios. One example is poly(*N*-isopropylacrylamide), a polymer with lower critical solution temperature properties,[15] whereby

K. Zhou, R. Sun, J. P. Wojciechowski, R. Wang, J. Yeow, Y. Zuo, X. Song, C. Wang, Y. Shao, M. M. Stevens
Department of Materials
Department of Bioengineering
and Institute of Biomedical Engineering
Imperial College London
London SW7 2AZ, UK
E-mail: molly.stevens@dpag.ox.ac.uk
M. M. Stevens
Department of Physiology
Anatomy and Genetics
Department of Engineering Science
and Kavli Institute for Nanoscience Discovery
University of Oxford
Oxford OX1 3QU, UK

The ORCID identification number(s) for the author(s) of this article can be found under https://doi.org/10.1002/adma.202312135

DOI: 10.1002/adma.202312135

an increase in temperature decreases solvation and initiates hydrophobic collapse of the polymer.[15b,16] Another example is poly(acrylic acid), a pH-responsive material where electrostatic repulsion of carboxylate groups varies with pH and effects the network density of the hydrogel.[4a,17] Hydrophobic polymers are also extensively investigated in soft actuators,[18] such as liquid crystal elastomers[19] whose deformations are caused by a change in liquid crystal phase initiated by a change in temperature.[20] Another class of materials are shape memory polymers (SMPs) which are materials that can fix a temporal shape deformation, then recover to their original shape.[21] These materials have shown adjustable actuation configurations using the transitions from a temporarily defined shape to the original shape, and by variability in their stiffness.[5a,22] Additionally, when embedded with functional nanoparticles, SMP based actuators can achieve untethered control by the use of light as a trigger.[23]

Whilst a range of stimuli have been demonstrated to trigger a soft actuator, often a single stimulus is used which can result in off-target initiation of the actuation upon sensing the environmental stimuli, or the actuation precision is fully relied on operator judgement without the ability to receive environment feedback for verification. Exploring multiple materials into one system is a feasible approach to improve the number of functionalities of SAs, however, these materials need to be separated such that their functions can act separately.[24] Additionally, using multiple stimuli enables the design of a system where global deformation can be controlled using logic gates, such that a combination/exclusion of particular stimuli is required, thus expanding the diversity and selectivity of the actuation mechanisms. This configuration results in a more controlled actuation within the intended site, which is challenging for a SA activated by a single stimulus to achieve.

Herein, inspired by multilayer printed circuit boards (PCB), we describe the development of a 4D printed multimaterial soft actuator (MMSA), which has advantages on fabrication methods and actuation mechanisms (Table S1, Supporting Information). We utilize masked stereolithography apparatus (mSLA) 3D printing (**Figure 1**) to assemble two different stimuli responsive materials systems, namely a hydrophilic pH-responsive hydrogel (pHGel) and a hydrophobic iron oxide nanoparticle (Fe_3O_4 NPs) embedded shape-memory polymer (FeSMP). A facile approach is introduced to bond these two materials via a single adhesive shape memory polymer layer which forms a hydrophobic interaction with the FeSMP layer and covalent bonds with the pHGel layer through a thiol-ene and Michael addition reactions (Figure 1b). To precisely control the actuation site and time of the MMSA, actuation only occurs when triggered by near-infrared (NIR) light, and in the correct pH environment, demonstrating dual-stimuli control (i.e., AND logic), where the dual-stimuli control is a method for dual authentication of operator judgement and environment feedback. This allows for decoupling of motion and actuation of the MMSA to achieve precise spatiotemporal control of actuation, which is the unique advantage of our system. The multilayered configuration facilitates a variety of functions including movement, sensing, and programmed actuation only in the presence of two stimuli (i.e., pH and temperature). We validate the functions of each component and optimize the fabrication techniques to prevent delamination of the layers, whilst allowing for controlled motion and actuation. The assembled MMSA demonstrates a spatially and temporally controlled actuation strategy based on this design concept, which exhibits the potential of 4D multimaterial printing.

2. Results and Discussion

2.1. Design and Fabrication of the Multimaterial Soft Actuator

We designed the multimaterial soft actuator (MMSA) with the ability to systematically introduce multistimuli responsiveness into a soft actuator. To achieve this, a three-layer device design is used to isolate each layer. This enables the fabrication of layers that can respond to stimuli independently of each other which gives greater control to the location and timing of an actuation. In our configuration, the FeSMP layer controls movement of the device via an external magnetic field and enables spatial triggering of actuation, initiated by a local increase in temperature via a photothermal effect with near-infrared (NIR) light. The middle, adhesive layer acts as the backbone to link the FeSMP and pHGel layers, whereas the pHGel layer serves as a pH sensitive layer which can swell in response to a pH change, but only actuates when the FeSMP layer is heated over its glass transition temperature, T_g (Figure 1d).

The FeSMP layer is composed of a validated SMP network[25] embedded with iron oxide (Fe_3O_4) nanoparticles that can be heated locally upon irradiation with NIR light via a photothermal effect. The Fe_3O_4 nanoparticles also allow for movement of the device in the presence of an external magnetic field (Figure S1a, Supporting Information). We use a SMP polymer with a glass transition temperature (T_g) greater than room temperature (20 °C) which maintains its shape until being triggered by NIR light. The middle, adhesive layer is a SMP that contains a three-arm thiol (trimethylolpropane *tris*(3-mercaptopropionate)), which introduces a covalent thioether bond through a thiol-ene reaction, allowing for a stable interface between the hydrophilic (pHGel layer) and the hydrophobic layers (FeSMP layer). Whilst possible to directly link the FeSMP and pHGel layers via a thiol-ene reaction, a two-layer design means that the FeSMP layer cannot be postcured independently of the pHGel layer after printing. Postcuring the FeSMP layer is crucial to the material properties of the layer, as the degree of crosslinking defines the T_g required for deformation, and hence allows for the actuation event to be triggered spatially. Attempts to postcure the FeSMP layer prior to printing of the pHGel layer in a two-layer configuration led to poor adhesion of the two materials, presumably due to the loss of reactive vinyl groups on the surface. Additionally, when the pHGel layer is postcured, the increased crosslinking density limits the swelling ratio of the hydrogel (vide infra), and the actuation ability of the materials are diminished. The three-layer design overcomes these challenges, because the middle adhesive layer acts as an interface between the FeSMP and pHGel layers. We designed the pHGel layer based on the copolymerization of acrylic acid (AAC), acrylamide (AM), and *N,N'*-methylene*bis*(acrylamide) (Bis), resulting in a hydrogel with a high swelling ratio in response to changes in pH.[26] With this design and material choice, we can achieve dual-stimuli trigger

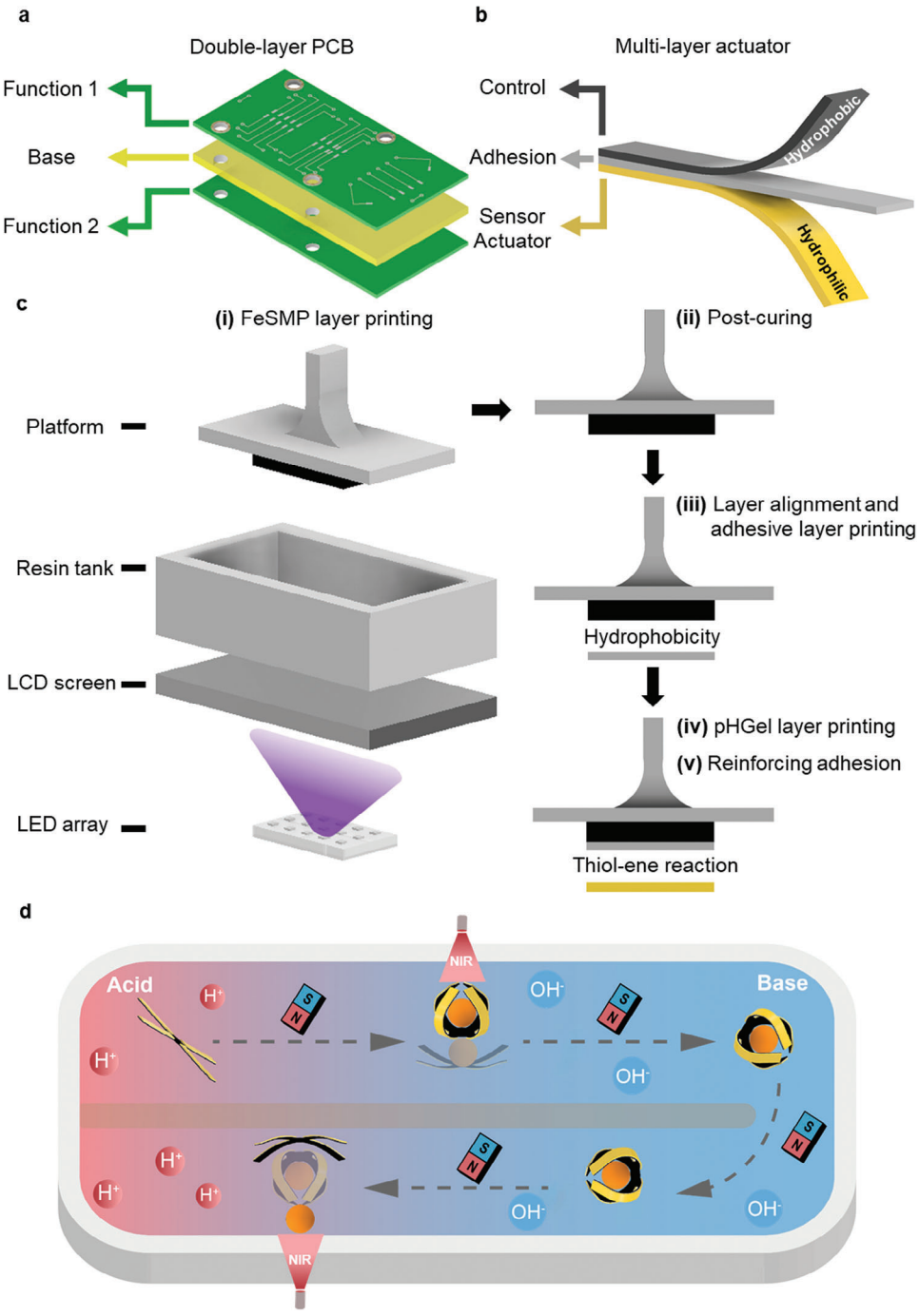

Figure 1. Schematic and fabrication of MMSA. a) Schematic of a double-layer PCB which has a substrate in the middle to link two separate functional layers. b) Schematic of the trilayer MMSA that integrates motion control, sensing, and actuation into one system with the aid of an adhesion layer in the middle. (c) MMSA fabrication method using a mSLA-based 3D printer. The key fabrication steps are: i) a FeSMP layer is printed on the platform, ii) the FeSMP attached to the platform is postcured, iii) an adhesive layer is printed on the surface of the FeSMP, iv) a pHGel was printed on adhesive layer and the thiol-ene reaction formed covalent bond to secure the attachment, v) to secure the formation of covalent bond, the printed MMSA was allowed to react in air overnight. d) Schematic of the MMSA working mode: The MMSA is designed to be magnetically directed from an acidic to an alkaline environment. Once in the alkaline environment, precise actuation occurs upon exposure to NIR light, enabling the MMSA to capture the target. With the target secured, the MMSA can then be magnetically guided back to an acidic environment. At this assigned position, the target is released upon a second exposure to NIR light.

actuation for increased spatial and temporal control of the actuation.

The MMSA is fabricated using a masked stereolithography apparatus (mSLA) 3D printer in a layer-by-layer manner. To fabricate the MMSA, there are five key steps (Figure 1c). i) Initially, the FeSMP layer is 3D printed. ii) While still attached to the printing platform, the FeSMP layer is postcured in a 405 nm light box at 60 °C for eight hours. Postcuring is performed prior to printing the subsequent layers to increase the crosslinking density of the FeSMP polymer network, and consequently define the initial geometry of the soft actuator (Figure S1b, Supporting Information). We found that prolonged heating and postcuring at 405 nm was required to completely polymerize the FeSMP material. After postcuring, reactive vinyl groups on the surface of the FeSMP layer were consumed as determined by FTIR (Figure S2b, Supporting Information), which led us to conclude that the bonding between the FeSMP and adhesive layer is mainly due to non-covalent interactions, although we cannot disregard the possible embedding of the FeSMP layer within the adhesive layer via swelling. The prolonged postcuring should not be harmful to polymers since the wavelength is within the range of visible light. To further substantiate this point, we tested samples with varying postcuring times using FTIR (Figure S3, Supporting Information). The spectra did not reveal any clear indications of polymer chain breakage, leading us to conclude that the postcuring process does not cause any significant damage to the material. iii) With the postcured FeSMP layer attached to the printer platform, the middle adhesive layer was printed onto the FeSMP layer after adjustment of the *z*-axis. iv) The pHGel layer was then printed onto the adhesive layer. Since the adhesive layer forms covalent bonds with the pHGel layer, a strong interface is formed between the two layers. v) The complete MMSA device is detached from the platform and allowed to stand at room temperature overnight. This step helps to avoid delamination during actuation, as we noticed delamination of the two layers if used immediately after printing (Figure S9, Supporting Information). We presume that the formation of stronger interfacial adhesion is due to the slow formation of covalent bonds via Michael addition reactions between reactive α,β-unsaturated carbonyls and the thiols present in the adhesive and pH gel layers.

2.2. Single Material Characterization and Formulation Choice

Before printing the MMSA, it is important to choose a material composition which has suitable photocuring properties for 3D printing and stimuli-responsive properties for actuation. We initially screened material compositions of the FeSMP and pHGel layers using in situ photorheology. The actuation ability of the pHGel layer depends on hydrogel swelling ratios, hence the crosslinking of the network is a key parameter. We use *N,N'*-methylenebis(acrylamide) (Bis) as a crosslinker for the hydrogels, as the concentration of Bis can be used to control the hydrogel swelling ratio. For the pHGel layer, there is an optimal ratio of crosslinker to monomer where the swelling ratio of the hydrogel layer is high enough to allow for actuation, whilst simultaneously being stiff enough to actuate the FeSMP layer when heated past the T_g. Based on these considerations, five pHGel formulations with different Bis concentrations (1%, 3%, 5%, 7%, and 9% (weight of Bis/weight of the sum of AAC and AM)) were tested for hydrogel swelling (**Figure 2**a, and Figure S4, Supporting Information). The results meet the expectation that a higher concentration of Bis leads to a lower swelling ratio due to an increase in crosslinking density of the hydrogel network. The increase in the concentration of Bis was accompanied with an increase in crosslinking kinetics of the hydrogels, demonstrating an increase in the slopes of the linear region of the time-dependent storage modulus (*G'*) curves measured by in situ photorheology (Figure 2b). Based on the swelling and rheology results, 5% (w/w) Bis was chosen for 3D printing since it offered a good balance between hydrogel printability and swelling ratio.

For the FeSMP layer, the key parameter is the concentration of iron oxide nanoparticles, as this directly affects a plethora of properties such as: the photothermal effect, magnetism, mechanical properties, material homogeneity, and UV-curing efficiency. Increasing the concentration of nanoparticles resulted in a faster response to the applied magnetic field, and rate of the photothermal effect, but decreased the transparency of the material which decreased the crosslinking efficiency of FeSMP layer (Figure S5, Supporting Information). Because the Fe_3O_4 nanoparticles are more dense than the SMP resin, they settle with time in the resin and their distribution within the resin becomes heterogeneous with prolonged printing time. Moreover, the nanoparticles decrease the crosslinking density in the SMP network since their incorporation increases the distance between polymer chains, which will affect the T_g of the material. Because the shape-memory properties and the photothermal effect are essential for the MMSA, the influence of nanoparticle concentration on these properties was investigated. The shape recovery of five different concentrations (0%, 1.5%, 2.5%, 3.5%, and 4.5% (w/w) of Fe_3O_4 nanoparticles in SMP resin) was compared after excitation with 850 nm NIR light (Figure 2c, and Figure S6, Supporting Information) (Figure S7a, Supporting Information). Given that the SMP layer without Fe_3O_4 nanoparticles has no photothermal effect, this sample was used as a negative control as it cannot return to its initial flat shape after NIR light irradiation. Compared to the SMP without Fe_3O_4 nanoparticles, the four FeSMP candidates exhibited a photothermal effect, as evidenced by a change in shape, with the higher concentration of nanoparticles improving the recovery speed. It is worth noting that batch-to-batch variation is a challenge since the distribution of larger iron oxide nanoparticle aggregates in the SMP resin is not homogeneous (Figure S7a, Supporting Information). Furthermore, the shape recovery tests showed that all samples from the five different concentrations have shape-memory function at room temperature. According to these results, a concentration of 3.5% (w/w) Fe_3O_4 NPs in the FeSMP is a compromise between material properties and fabrication efficiency. To validate the shape-memory function, the T_g was measured by differential scanning calorimetry (DSC), demonstrating (Figure S1a, Supporting Information) that compared to SMP, FeSMP has a broader glass transition temperature which is also lower than the T_g of SMP but higher than room temperature which supported the existence of shape-memory function.

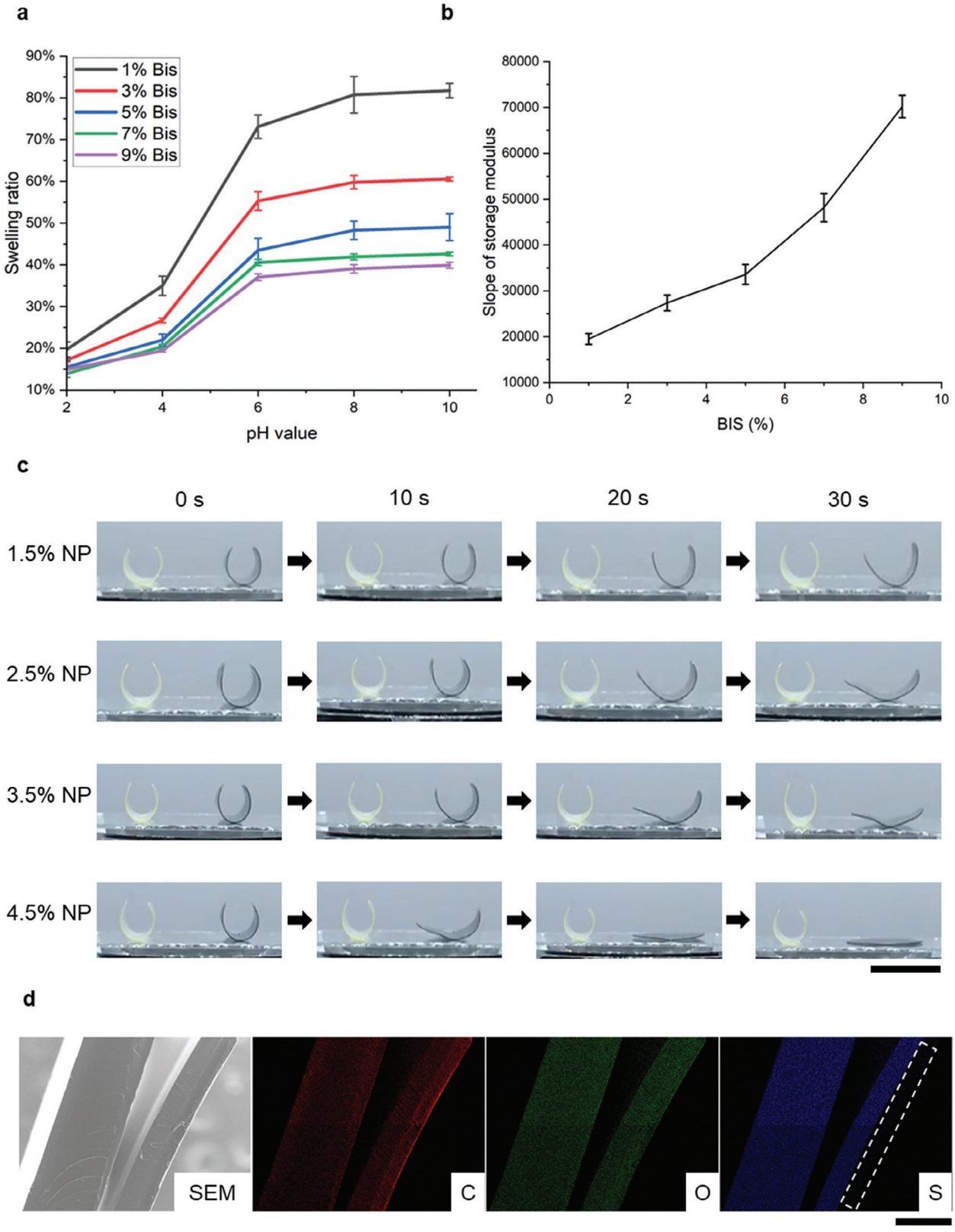

Figure 2. SA formulation and adhesion validation. a) Swelling ratio of pHGel candidates with different Bis concentrations soaked in pH buffers. Mean ± S.D., $n = 4$. b) The slope of storage modulus (G′) linear change part in different pHGel candidate rheology curves ($n = 3$). c) Photothermal effect test based on shape recovery with NIR LED (850 nm) exposure for FeSMP candidates with different nanoparticle concentrations at different time points. Scale bar: 20 mm. d) SEM image and EDS elemental mapping of carbon (C), oxygen (O) and sulfur (S) of a trilayer MMSA cross-section, whereby the dotted area represents the invisible pHGel layer in the S element mapping. Scale bar: 400 µm.

2.3. Multimaterial Printability and Layer-to-Layer Adhesion

The multilayer structure of the MMSA uses different materials to create multiple stimuli responsive layers. It was therefore important to confirm the printing fidelity and resolution of the various materials. To validate the printing fidelity, we printed an array of cylinders that were 1 mm in height with varying diameters ranging from 200 to 800 µm (Figure S8a, Supporting Information). In all three layers the 200 µm diameter cylinder was not produced, showing only tiny debris from failed printing. Cylinders with a diameter equal to and greater than 300 µm were successfully printed for all layer compositions with acceptable errors (Figure S8b, Supporting Information). For the pHGel layer, there was a small amount of overcuring at the interface between the substrate and cylinders. This overcuring only existed at the interface and is likely due to trapped resin between the initially thin layers and the substrate. In practice, because the FeSMP layer or SMP layer will be printed first, this should not affect the printing fidelity of the resulting MMSA devices. This indicates a smallest feature size of ≈300 µm which is more than sufficient for the design of soft actuators which are typically on the centimeter scale.

The layer-to-layer adhesion was also a crucial parameter as it directly affects the operation of the actuator. The bonding mechanism between the FeSMP layer and the adhesive layer is due to noncovalent interactions, with the interface being reliable in an aqueous working environment due to the hydrophobicity of the two layers. In contrast, the linkage between the hydrophobic adhesive layer and the hydrophilic pHGel layer is a covalent bond. This is required to prevent pHGel layer delamination from the adhesive layer because of the mismatch in surface chemistry. To confirm a stable bond was formed between the two interfaces, the pHGel layer was printed onto the adhesive layer under two experimental conditions: i) where the adhesive layer was postcured before printing, and ii) when the adhesive layer was not postcured. The dual-layer structures were cut to observe the cross-section by scanning electron microscopy (SEM) (Figure S9, Supporting Information). The postcured adhesive layer does not bond with the pHGel layer, revealing a gap between the interfaces at the cross-section upon cutting. In contrast, when the pHGel layer was directly printed without postcuring, the bond between the layers was strong enough to resist the shear force from the cut. A further investigation of the reaction time was conducted by cutting the sample at different time points (Figure S9, Supporting Information). When the dual layer structure was immediately cut after printing, a small gap was observed with the postcured sample, while the sample left for 12 h showed an interface that was fused and remained intact. We can infer from these results that whilst the thiol-ene reaction occurs during the printing process, a Michael addition between thiols in the SMP layer and α,β-unsaturated carbonyls in the pHGel layer likely reinforces the interface between the adhesive layer and pHGel layer after printing. The combination of the two reactions act together to overcome incompatibility between a hydrophilic and a hydrophobic material.

To directly compare the difference of the two adhesion mechanisms, a strip of trilayer MMSA was cross-sectioned, and the layer interface was inspected using SEM (Figure 2d). There was an apparent gap between the FeSMP and the adhesive layer since the weaker, noncovalent bonds adhering these layers cannot bear the shear stress caused by the cutting, while the adhesive layer remained attached to pHGel layer. We further confirm the identity of the layers using EDS elemental mapping since the pHGel does not contain sulfur, which shows the lower intact adhesive and pHGel layers are still bonded.

2.4. Anisotropic Designs for Creating Diverse Actuation Models

We next exhibit various modes of actuation by the design of the MMSA. Three different MMSA structures (i.e., strip, gripper, and clover) were printed to investigate various modes of actuation. When immersed in buffered aqueous solutions at 45 °C, each structure displayed distinctive actuation modes (**Figure 3**a). The trilayer strip exhibited a bending actuation, where the degree of deformation increased as the pH increased. The recovery of the bending actuation was induced by decreasing the pH or dehydration in air at 60 °C (Figure 3b). The actuation and recovery revealed the potential of cycling uses of MMSA which can further enhance the application potential, so a cycling test on trilayer strip MMSA was conducted to demonstrate the duration (Figure S10, Supporting Information).

More complex structures were created according to two categories of designs. The first design is based on the distribution of the pHGel layer, where the adhesive and the pHGel layers were selectively printed onto the FeSMP layer. The other design is based on utilizing the greyscale value[27] of the photomask in the 3D printer to modulate the UV exposure strength, and ultimately affect the crosslinking density of the pHGel network. This has the effect of varying the swelling ratios of the pHGel layer, and hence degree of force applied to the actuation. To demonstrate spatial control of the pHGel layer, we printed a gripper structure comprising three trilayer strips bonded to a FeSMP base layer. When the pHGel layer is distributed homogenously throughout the MMSA, the structure does not actuate. In contrast, a heterogenous distribution of the pHGel layer on the structure facilitated a graded actuation that operated as a gripper (Figure 3c). The clover-like structure exhibited a more complex twisting actuation that was programmed by the alignment of the pHGel layer being orthogonal to the axis of the clover branches (Figure 3d). We additionally demonstrated differences in network density using greyscale values to control the deformation of the clover-like structure. For the three strips of pHGel on each leaf, the UV exposure could be homogenous or heterogeneous. For the heterogenous strips, greyscale gradients of 0%, 25%, and 50% from center to the edge were fabricated. The comparison of the two distributions showed that with the increasing greyscale gradients, the twisting actuation of leaves was more pronounced (Figure 3e). The difference between the homogenous and heterogeneous samples reflects that the varied greyscale values can alter the swelling ratio of the pHGel layer and hence the actuation of each strip.

Our MMSA design requires both stimuli (i.e., pH and temperature) to initiate actuation. To illustrate the advantages of the photothermal properties within the FeSMP layer, two actuators in aqueous buffer solution (pH = 10), activated by different light sources demonstrated complex actuation control. Initially, when

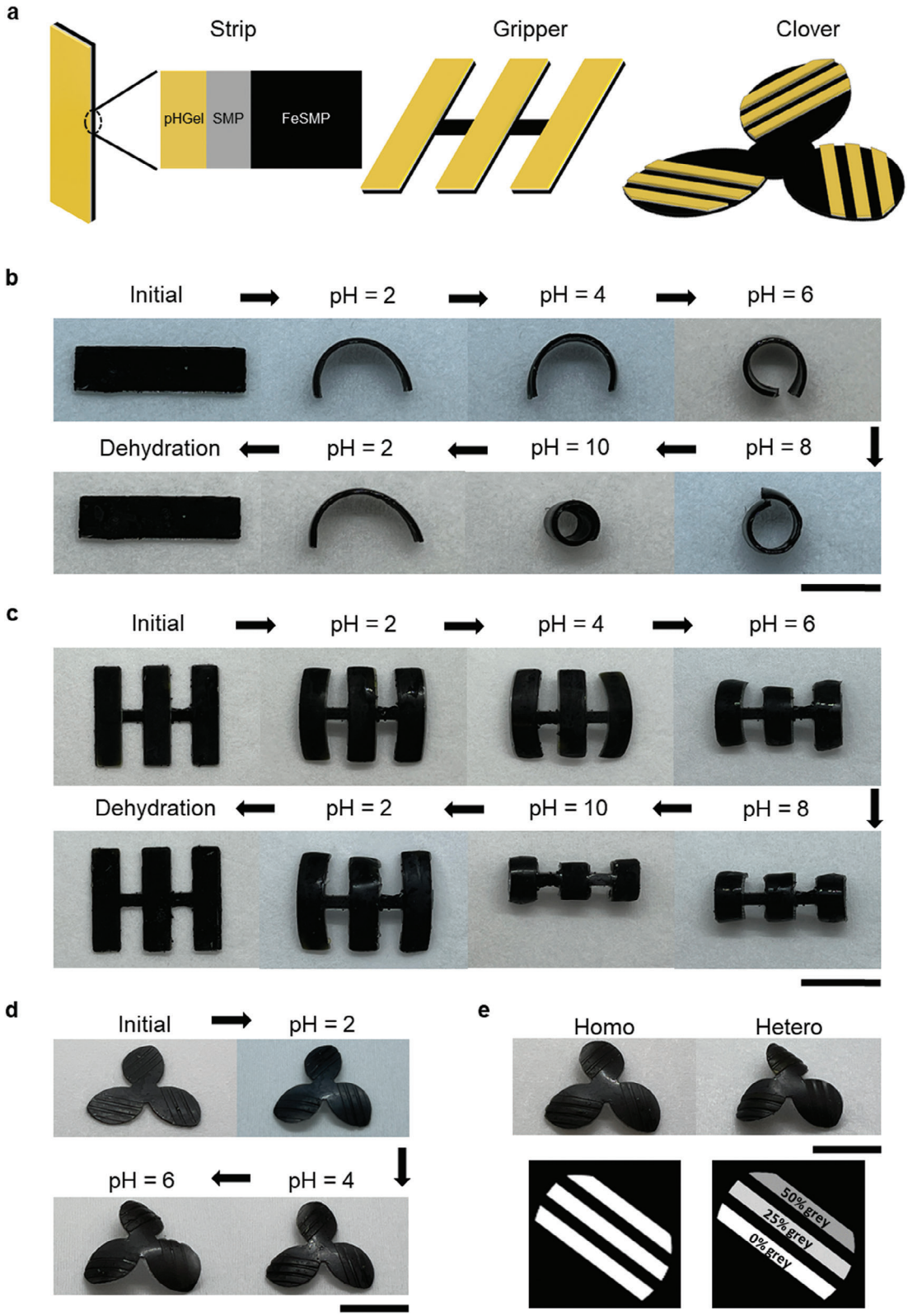

Figure 3. Actuation patterns of 3D printed anisotropic structures in buffer solution at 45 °C. a) 3D models of three structures: strip, gripper, and clover. b) Strip MMSA actuation in 45 °C buffers and dehydration at a hot plate. c) Gripper MMSA actuation in 45 °C buffer and dehydration at a hot plate. d) Clover MMSA exhibited twisting actuation in 45 °C buffers. e) The exposure to homogeneous and heterogeneous UV-curing led to different actuations activated in 45 °C DI water. The pHGel layer sliced pictures whereby the left bottom one without grey scale and the right bottom one with grey scale design. Scale bar: 10 mm.

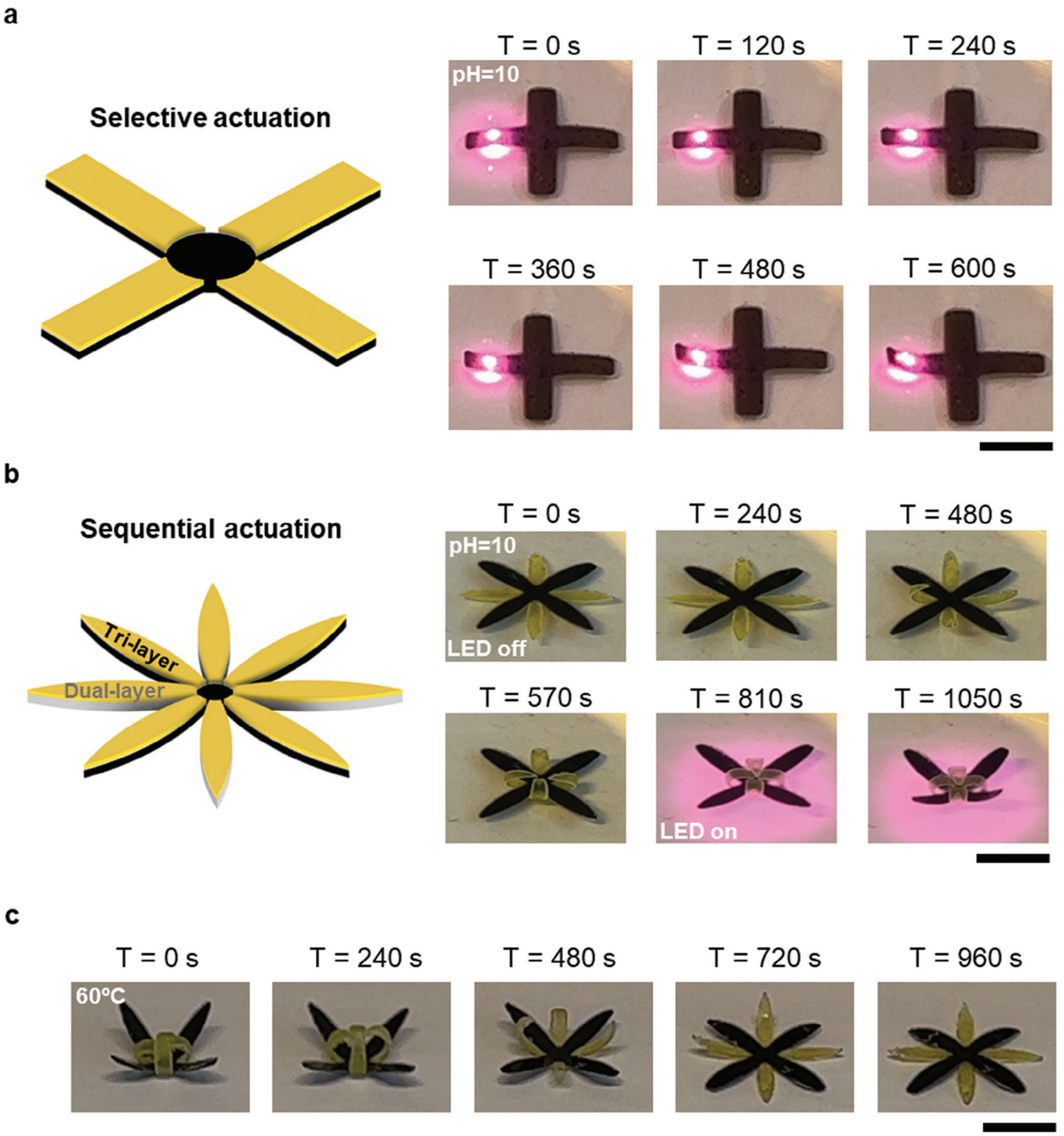

Figure 4. Untethered control of MMSA activation by NIR light stimulation. a) NIR laser selective activation with of one arm of a 4-arm MMSA results in pH change sensing and actuation. b) Sequential actuation of 8-arm MMSA, with 4-arm dual layer spontaneously actuating in pH 10 buffer and 4-arm trilayer actuating with the global exposure of NIR LED in pH 10 buffer. c) The dehydration and recovery of 8-arm MMSA on a hot plate. Scale bars: 10 mm.

the 4-arm gripper structure was immersed into buffer solution (pH = 10) at room temperature, no actuation occurred because the FeSMP layer was not heated above its T_g. When an 808 nm NIR laser was focused onto one arm of the structure, the local temperature increases via a photothermal effect caused actuation of the arm whilst the other arms remained unchanged (**Figure** 4a). Selective actuation represents the potential to reprogram the configuration of the actuator in response to an event. To highlight this, chronologically focused stimulation was shown to selectively control different parts of the structure. An 8-arm

claw structure was fabricated with alternating arms possessing an FeSMP layer or a SMP layer. The SMP layer has a dual-layered composition of adhesive and pHGel, which spontaneously actuated once immersed in buffer solution (pH = 10). Under 850 nm NIR LED irradiation, the FeSMP-arms were selectively actuated (Figure 4b). The sequential actuation of the MMSA demonstrated the advantage of a trilayer structure with a controllable actuation in the working pH environment. In the pH 10 buffer, the trilayer MMSA can be precisely controlled to actuate at a specific site and time point due to active control imparted by the photothermal effect from the FeSMP layer. Compared with the trilayer structure, the dual-layer actuated immediately in the pH 10 buffer which cannot achieve precise spatiotemporal control.

2.5. Function Integration to Achieve Spatially and Temporally Controlled Actuation

The integration of movement, sensing, and actuation was demonstrated in a capture-release scenario to show the advanced functions of the MMSA (**Figure 5**). A 4-arm gripper MMSA was printed to execute the capture and release of a ball (diameter = 5 mm). i) In a pH 10 buffer, the gripper started to wrap the ball under NIR stimulation. ii) With the ball captured, the gripper was taken out from the buffer using a magnet to complete the target capture process. iii) The magnet guided the loaded gripper to move in a pH 2 buffer from the starting site to the proposed site such that pH change could induce the shrinkage of pHGel. iv) Excitation with NIR light triggered actuation of the FeSMP layer to open the gripper structure, releasing the ball. v) The magnet collected the gripper from the buffer to separate the gripper and the ball. In this demo, the active spatial and temporal control of the actuation was exhibited since the operator could control the movement and release independently.

The dual-stimuli control strategy can achieve active precise spatiotemporal actuation, and the response time of the multimaterial soft actuator (MMSA) can be easily adjusted to meet practical requirements, particularly in scenarios where a rapid response is essential. The response time is affected by the glass transition temperature and heating rate of the FeSMP layer, and the swelling rate of the pHGel layer. Both rates can be significantly increased with a thinner design and a higher thickness ratio of the pHGel layer to the FeSMP layer (Figure S11, Supporting Information). Compared to the original design which has a FeSMP layer that is 0.5 mm thick, a thinner FeSMP layer that is 0.25 mm thick, heated up and softened more rapidly. After three minutes of NIR light exposure, there was obvious bending, whilst the original design only deformed a small amount in this timeframe. A thinner FeSMP layer requires less thermal energy to reach its glass transition temperature, thereby shortening the response time. Similarly, a less thick pHGel layer can swell faster due to a higher surface area for water absorption. Combined with a thinner FeSMP layer of 0.1 mm and a pHGel layer of 0.05 mm, the MMSA deformed significantly faster after 180 seconds. Additionally, a higher thickness ratio of the pHGel layer to the FeSMP layer proved effective in improving the response speed of the MMSA, where the MMSA with both an FeSMP and pHGel layers of 0.1 mm thickness deformed the most in the timeframe compared to other samples, as it enhances the force generated from swelling to overcome constraints from the FeSMP layer. The comparison between the last two samples (iii and iv) infers that there could be an optimization of pHGel layer thickness to achieve fastest actuation.

Apart from thickness adjustment of the FeSMP and pH layers, there are two other possible methods to increase response rate. Increasing the actuation driving force can be achieved by: adopting a lower pH value, increasing the working environment temperature, or using stronger NIR illumination. These approaches aim to enhance the swelling force of the pHGel and reduce the heating time of the FeSMP layer through more intense stimuli. However, this method is relatively demanding for the working environment. Altering the chemical composition of the MMSA could be another effective method to reduce response time. This can be done by increasing the number of photothermal nanoparticles in the FeSMP layer or incorporating them into the adhesive layer, which improves the photothermal effect for a faster increase in temperature. Furthermore, the ratios of monomers can be varied to lower the glass transition temperature of the FeSMP layer, reducing the time required to reach the glass transition temperature which results in a faster actuation response.[25] Enhancing the sensitivity to pH changes and the mechanical properties of the pHGel can also contribute to a more rapid response. This can be achieved by increasing the concentration of acrylic acid or adding metal ions to the pHGel formulation, which helps to more quickly overcome the constraints imposed by the FeSMP.[28]

3. Conclusions

Herein we developed a fabrication method for a multimaterial soft actuator comprising a hydrophilic pH-responsive hydrogel, an adhesive layer, and a hydrophobic shape-memory polymer. Our fabrication approach enabled the design of a soft actuator which requires multiple stimuli to trigger the actuation (i.e., AND logic) and overcomes challenges in material compatibility with an adhesive layer. We show that using 3D printing, we can design a variety of actuation patterns through geometric changes, spatial control of stimuli responsive layers, and controlled crosslinking using grayscale photomasks. In our design of the MMSA, we use iron oxide nanoparticles embedded in the hydrophobic shape-memory polymer layer to control movement of the device via an external magnetic field and to introduce spatial control in the actuation via local heating when irradiated with NIR light through the photothermal effect of the iron oxide nanoparticles. In combination with the pH-responsive hydrogel layer, we show that actuation only occurs in the correct environmental pH conditions, demonstrating dual-stimuli control of the actuation.

We demonstrate the potential of the MMSA in a range of applications such as a typical capture and release test demonstrating that the MMSA could be precisely controlled to actuate via the combination of external stimuli. We envisage the facile design of the MMSA can be applied to other soft actuators to enable increasingly complex stimuli-responsive mechanisms and overcome a key challenge of material interface connection in the design of multifunctional soft actuators. We hope the increased spatial and temporal control of the soft actuator can ultimately be applied in a range of fields, such as smart drug delivery systems

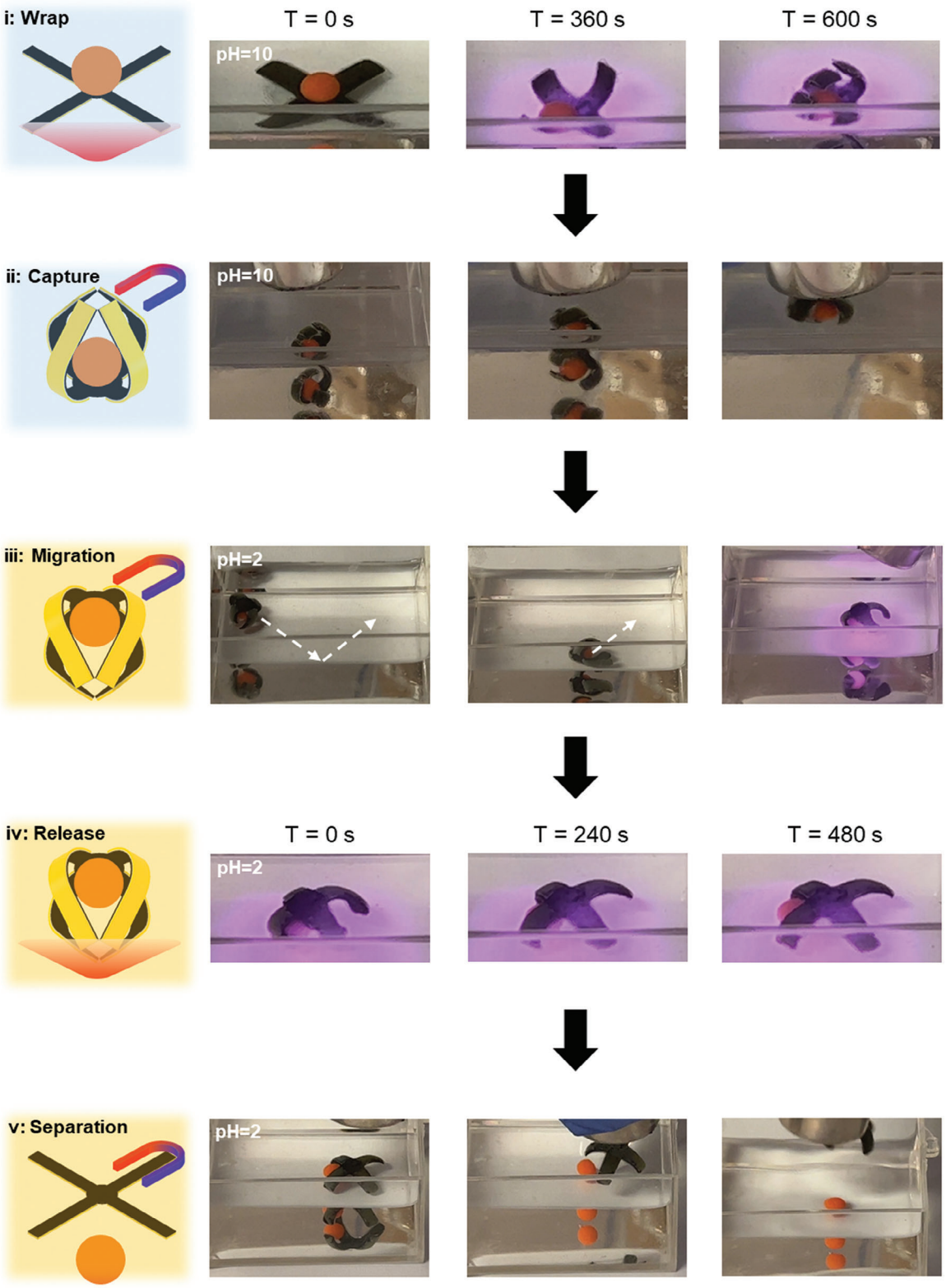

Figure 5. Demonstration of capture and release capability of a 4-arm MMSA with spatiotemporal control. i) A 4-arm MMSA wrapped the ball in pH 10 buffer when NIR LED was on. ii) A magnet was used to capture the MMSA from the buffer. iii) To release the ball, the MMSA was magnetically guided in pH 2 buffer along the direction marked by dotted lines to a target position. iv) The target position where the NIR LED was set beneath, was the release site. Release was activated in the target position by NIR LED exposure. v) After the release, the MMSA was collected by the magnet to achieve cargo and carrier separation. Scale bar: 10 mm.

in soft robotics, biomedical engineering for the manipulation of tissue or environmental engineering.

4. Experimental Section

Materials: All chemicals and reagents were directly used without any further processing. The chemicals are acrylamide (AAM, Sigma-Aldrich A3553), acrylic acid (AAC, Sigma-Aldrich 147230), *N*,*N*′-methylene-*bis*(acrylamide) (Bis, Sigma-Aldrich 146072), lithium phenyl(2,4,6-trimethylbenzoyl)phosphinate (LAP, TCI UK L0290), pure water (Millipore Milli-Q Integral 3), tartrazine (Instant Sunshine), poly(ethylene glycol)methyl ether (mPEG, Sigma-Aldrich 202509, Mn 2000), 1,3,5-triallyl-1,3,5-triazine-2,4,6(1H,3H,5H)-trione (TATATO, Sigma-Aldrich 114235), *tris*(3-mercaptopropionate) (TMTMP, Sigma-Aldrich 381489), tricyclon[5.2.1.$0^{2,6}$], decanedimethanol diacrylate, (TCMDA, Sigma-Aldrich 496669), 2,5-bis(5-*tert*-butyl-benzoxazol-2-yl)thiophene, (OB^+, Sigma-Aldrich 223999), 2-benzyl-2-(dimethylamino)-4′-morpholinobutyrophenone (I-369, Sigma-Aldrich 405647), and iron (II, III) oxide (Sigma-Aldrich 637106). Isopropanol (IPA, Fisher Chemical P/7500/17), acetone (VWR 20066.330), pH 2, 4, 6, 8 and 10 Buffer solutions (Sigma-Aldrich 1094331000, 1094351000, 1094371000, 1094601000, and 1094381000), and Prusament Resin Tough Prusa Orange (Prusa Research) were used.

Printing Formulations: The SMP formulation consists of 1.78 g TATATO, 1.89 g TCMDA, 2.75 g TMTMP, 12 mg I-369, and 6 mg OB^+. The FeSMP layer consists of the SMP formulation and 222.6 mg of iron (II, III) oxide NPs. The pHGel layer consists of 4 g AAM, 2 mL AAC, 300 mg Bis, 2 mL ultrapure water, 30 mg LAP, 12 mg tartrazine, and 500 mg mPEG.

Single Layer Material Preparation: Single layer materials were fabricated in a rheometer (Antor-Paar MCR 302) with a stainless-steel measuring plate of 25 mm diameter, glass plate with peltier control (P-PTD 200/GL) and with an installed UV light source (OmniCure series 1500). To fabricate the samples, 0.5 mL solutions of different formulations were aliquoted under the measuring plate, the plate lowered, then extra solution was removed when the gap between the measuring gap reached 0.2 mm. There were two intervals in one curing process: the first interval was without UV light to reach a stable state; then UV was on to initiate the curing. During the UV curing process, the shear strain was 0.1% and the angular frequency was 6.28 rad s^{-1}.

Cured samples detached from the measuring plate and they were punched into 20 mm diameter discs, and every disc had the same size of 20 mm diameter and 0.2 mm thickness for following comparison experiment. Moreover, the samples of SMP and FeSMP candidates were postcured in a light box ($\lambda = 405$ nm) at 60 °C for 8 h.

pHGel Candidates Swelling Test: pHGel candidate samples were soaked in pure water for 12 hours to wash away extra monomers and other free components inside. Then the samples were soaked in pH buffers to reach saturation. Size changes of the samples were measured by grid papers with the unit size of 0.2 mm.

Shape-Memory Function Test: The samples of FeSMP candidates and SMP were heated to 45 °C on a hot plate. The heated samples were wrapped around a glass tube with 0.7 mm outside diameter to form a temporary curvature. The curved samples were allowed to cool down in air to fix the shape, and these samples recovered to the original shapes by reheating on a 45 °C hot plate.

Photothermal Property Test: FeSMP candidate samples and SMP samples were processed following the same procedure as in the shape-memory function test. The samples were placed on a glass slide and exposed to a LED array (850 nm, ILR-IO09-85NL-SC201-WIR200), to induce a photothermal effect in room temperature.

Tensile Tests: pHGel, SMP, and FeSMP materials were printed into dumbbell structures (ASTM D412). The pHGel and FeSMP samples were 0.125 mm thick and the SMP samples were 0.1 mm thick. The FeSMP samples were postcured to be fully polymerized in a UV box (405 nm) at 60 °C for 8 h. Tensile tests were conducted on Mecmesin MultiTest-i with a 25 N sensor. The speed of displacement was 100 mm min^{-1}.

Differential Scanning Calorimetry: Less than 10 mg of SMP, UV cured FeSMP, and printed FeSMP samples, that all were postcured, were put into sample pans. A heat-cool-reheat process was conducted with a temperature change rate at 10 K min^{-1}. The samples were heated from 25 °C to 100 °C, cooled down to −20 °C, and reheated to 100 °C. The heat-cool-reheat experiment produced a clear reheat curve which was used to evaluate T_g. Printed FeSMP without postcuring cannot be reheated to 100 °C as this might induce further polymerization. Therefore, this sample was cooled from 25 to −40 °C and then heated to 60 °C with a temperature change rate of 10 K/min.

Fourier-Transform Infrared Spectroscopy (FTIR): Monomers of SMP printing formulation and printed FeSMP samples without and with different postcuring time were analysed by FITR spectroscopy (ALPHA II, Bruker). The monomers were measured with 24 scans and the printed FeSMP samples were measured with 128 scans.

Scanning Electron Microscope Imaging and Element Mapping: SEM samples were attached to the conductive tape on the top surface of sample holders and coated with 15 nm chromium with a pumped coater (Quorum, Q150T Plus). SEM imaging was conducted on a Zeiss Auriga with 5 kV voltage. Element mapping was conducted on the same machine with 20 KV voltage.

Multimaterial Printing: All 3D models were created at Inventor (Autodesk 2022), and STL files were exported for slicing. The STL files were imported into PrusaSlicer to create printing files. To print the MMSA, every material needed a printing file, so there were three printing files for each actuator. For the clover-like actuator and tensile tests samples with grey scale on pHGel, the pHGel printing files were converted to zip file which included pictures of UV mask for each slice. Using Photoshop (Adobe 2019) to adjust grey scale of the picture, the heterogeneous clover-like actuator had a normal pHGel strip, a 25% grey pHGel strip, and a 50% grey pHGel strip from the center to the edge on every leaf. As for the tensile test samples, the grey scale was homogeneous, so there were 25% grey and 50% grey pHGel dumbbell pictures used for sample printing. Edited pictures by Photoshop were packed into the zip files and the files were converted to printing files ready for printing.

To print the MMSA, the printing order was from FeSMP, adhesive layer, and then pHGel. The slice thickness for all layers is 0.025 mm. i) A FeSMP layer was printed into a final thickness of 0.5 mm. The printing time of FeSMP was 120 s for the first slice, and the following were 60 s per slice. ii) Printed FeSMP attached to the printing platform was postcured in a light box (405 nm) at 60 °C for 8 h. iii) An adhesive layer needed to be printed on FeSMP layer, so the platform with FeSMP layer was calibrated on the printer to reset Z direction. With the new zero point at the surface on FeSMP layer, an adhesive layer was printed with the printing time of 60 s for the first layer and 40 s for the following, and the final thickness of adhesive layer is 0.1 mm. iv) Without any post process on adhesive layer, the platform was calibrated to reset Z direction again. Then pHGel was printed on adhesive layer to from trilayer structure. v) After printing, trilayer MMSA was ready to use after an overnight with reinforced adhesion between the adhesive layer and pHGel layer.

Actuation in 45 °C Buffers: Petri dishes with buffers were heated on a hot plate to 45 °C, which is a temperature higher than the T_g of FeSMP. Printed MMSA were put into 45 °C solutions for 2 min and taken out to cool down in air for observation.

Cycling tests in 45 °C Buffers: Petri dishes with pH 2 and pH 10 buffers were heated on a hot plate to 45 °C. Printed MMSA were put into the pH 10 solution for two minutes and taken out to cool down in air for observation, and then were put into pH 2 solutions with the same operation to observe actuation change. The operations above were repeated for 20 times on each sample.

NIR Induced Actuation in Buffers: A NIR laser (808 nm IR InfraRed at 0.6 W·cm^{-2}) was used to selectively heat one arm of the 4-arm claw MMSA that was soaked into pH 10 buffer at room temperature. The LED array (850 nm) was used to heat the 8-arm claw, which activated the 4 arms with FeSMP layer to actuate in pH 10 buffer at room temperature.

Capture and Release Demo: In a container with pH 10 buffer, a 4-arm claw MMSA holding a printed ball (diameter = 5 mm) was placed over

an area illuminated by an LED (850 nm) array. When the LED was on, the arms started to bend until they wrapped the ball. A magnet was used to take the claw and the ball out of the solution. Without the LED light, the claw cooled down fast and the deformation was fixed. To release the target, the claw was placed in a container with pH 2 buffer. Using a magnet, the claw was moved along the container to the specific position illuminated by the LED array. Then LED activated the claw to start releasing the ball in situ and the claw was collected using the magnet.

NIR Induced Actuation of Different Thickness MMSA in pH 10 Buffer: To verify that the actuation speed varied from the thickness of MMSA, 4 MMSA with different thickness designs were soaked into pH 10 buffer and heated by an LED array (850 nm).

Supporting Information

Supporting Information is available from the Wiley Online Library or from the author.

Acknowledgements

The authors acknowledge Dr. Akemi Nogiwa Valdez for extensive manuscript and data management support. The authors acknowledge access to SEM facilities at the Harvey Flower Electron Microscopy Suite (Department of Materials, Imperial College London), and confocal microscopy facilities at the Department of Bioengineering (Imperial College London). J.Y. acknowledges funding from the European Union's Horizon 2020 research and innovation programme under a Marie Skłodowska-Curie grant agreement (839137). R.W. acknowledge funding from The Rosetrees Trust under the Young Enterprise Fellowship agreement (A2741/M873). X.S. acknowledges the financial support from the China Scholarship Council. M.M.S. and J.W. acknowledge support from the grant from the UK Regenerative Medicine Platform "Acellular / Smart Materials – 3D Architecture" (MR/R015651/1). Y.S. acknowledges the support of the Natural Sciences and Engineering Research Council of Canada (NSERC). M.M.S. acknowledges support from the Royal Academy of Engineering Chair in Emerging Technologies award (CiET2021\94). For the purpose of open access, the author has applied a 'Creative Commons Attribution (CC BY) license to any Author Accepted Manuscript version arising.

Conflict of Interest

MMS invested in, consults for or was on scientific advisory boards or boards of directors, and conducts sponsored research funded by companies related to the biomaterials field. The rest of the authors declare no conflict of interest.

Author contributions

K.Z. and R.S. contributed equally to this work. K.Z. and R.S., and M.M.S. conceived and/or designed the research. K.Z and R.S. conducted the experiments. J.P.W., R.W., J. Y., Y.Z., X. S., C.W., and Y.S. contributed to data analysis and/or provided conceptual advice. All the authors discussed the results and assisted in the preparation of the paper. K.Z drafted the manuscript. J.P.W., R.W., J. Y., Y.Z., X. S., C.W., Y.S., and M.M.S. revised the paper. M.M.S. supervised the study. All authors have given approval to the final version of the manuscript.

Data Availability Statement

All data are available in the manuscript or the supplementary materials. Raw research data is available upon reasonable request from the corresponding author.

Keywords

4D multimaterial printing, photothermal effect, pH-responsive hydrogel, shape-memory polymer, soft actuator, spatial and temporal control, thiol-ene reaction

Received: November 14, 2023
Revised: January 16, 2024
Published online: February 11, 2024

[1] a) M. Li, A. Pal, A. Aghakhani, A. Pena-Francesch, M. Sitti, *Nat. Rev. Mater.* **2022**, *7*, 235; b) S. Kim, C. Laschi, B. Trimmer, *Trends Biotechnol.* **2013**, *31*, 23.
[2] M. Cianchetti, C. Laschi, A. Menciassi, P. Dario, *Nat. Rev. Mater.* **2018**, *3*, 143.
[3] a) Y. Kim, X. H. Zhao, *Chem. Rev.* **2022**, *122*, 5317; b) B. Han, Z. C. Ma, Y. L. Zhang, L. Zhu, H. Fan, B. F. Bai, Q. D. Chen, G. Z. Yang, H. B. Sun, *Adv. Funct. Mater.* **2022**, 32; c) W. Q. Hu, G. Z. Lum, M. Mastrangeli, M. Sitti, *Nature* **2018**, *554*, 81; d) M. Y. Razzaq, M. Behl, M. Heuchel, A. Lendlein, *Macromol. Rapid Commun.* **2020**, 41.
[4] a) D. D. Jin, Q. Y. Chen, T. Y. Huang, J. Y. Huang, L. Zhang, H. L. Duan, *Mater. Today* **2020**, *32*, 19; b) Z. L. Han, P. Wang, G. Y. Mao, T. H. Yin, D. M. Zhong, B. R. B. Yiming, X. C. Hu, Z. Jia, G. D. Nian, S. X. Qu, W. Yang, *ACS Appl. Mater. Interfaces* **2020**, *12*, 12010; c) A. S. Gladman, E. A. Matsumoto, R. G. Nuzzo, L. Mahadevan, J. A. Lewis, *Nat. Mater.* **2016**, *15*, 413.
[5] a) J. A. C. Liu, J. H. Gillen, S. R. Mishra, B. A. Evans, J. B. Tracy, *Sci. Adv.* **2019**, 5; b) J. K. Park, K. W. Nan, H. W. Luan, N. Zheng, S. W. Zhao, H. Zhang, X. Cheng, H. L. Wang, K. Li, T. Xie, Y. G. Huang, Y. H. Zhang, S. Kim, J. A. Rogers, *Adv. Mater.* **2019**, *31*, 1905715; c) S. K. Auer, S. Fossati, Y. Morozov, D. C. Mor, U. Jonas, J. Dostalek, *J. Phys. Chem. B* **2022**, *126*, 3170;. d) L. F. Chang, D. P. Wang, Z. S. Huang, C. F. Wang, J. Torop, B. Li, Y. J. Wang, Y. Hu, A. Aabloo, *Adv. Funct. Mater.* **2023**, 33.
[6] a) D. J. Jiao, Q. L. Zhu, C. Y. Li, Q. Zheng, Z. L. Wu, *Acc. Chem. Res.* **2022**, *55*, 1533; b) Herianto, I. Wira, R. A. Syahirul, P. Aishah, *Sens. Actuators A, Phys.* **2019**, *298*, 111556.
[7] a) Q. Ren, X. Sun, W. Liu, Z. Li, C. Jiang, Q. X. Hou, *Chem. Eng. J.* **2023**, 456; b) A. Le Duigou, V. Keryvin, J. Beaugrand, M. Pernes, F. Scarpa, M. Castro, *Composites, Part A* **2019**, *116*, 36.
[8] Q. Fu, H. B. Zhang, Z. M. Wang, M. Chiao, *J. Mater. Chem. B* **2017**, *5*, 4025.
[9] a) A. Zolfagharian, A. Z. Kouzani, S. Y. Khoo, A. A. A. Moghadam, I. Gibson, A. Kaynak, *Sens. Actuators, A* **2016**, *250*, 258; b) E. Kudryavtseva, V. Popov, G. Muller-Kamskii, E. Zakurinova, V. Kovalev, in Proc. of the 2020 IEEE 10th Int. Conf. on Nanomaterials: Applications & Properties (Nap-2020) **2020**; c) M. Attaran, *Bus Horizons* **2017**, *60*, 677.
[10] Y. Zhou, W. M. Huang, S. F. Kang, X. L. Wu, H. B. Lu, J. Fu, H. P. Cui, *J. Mech. Sci. Technol.* **2015**, *29*, 4281.
[11] a) D. M. Smith, Y. Kapoor, G. R. Klinzing, A. T. Procopio, *Int. J. Pharm.* **2018**, *544*, 21; b) J. A. Cone, T. M. Martin, D. J. Marcellin-Little, O. L. A. Harrysson, E. H. Griffith, *Am. J. Vet. Res.* **2017**, *78*, 900.
[12] H. Liu, R. A. Liu, K. Chen, Y. Y. Liu, Y. Zhao, X. Y. Cui, Y. Tian, *Chem. Eng. J.* **2023**, 461.
[13] a) S. Tibbits, presented at TED conference, **2013**; b) S. Tibbits, C. McKnelly, C. Olguin, D. Dikovsky, S. Hirsch, *Acad. Des. Agency* **2014**, *2014*, 539; c) S. Tibbits, *Delft Prog. Rep.* **2014**, *84*, 116; d) F. Momeni, N. S. M. M. Hassani, X. Liu, J. Ni, *Mater Design* **2017**, *122*, 42; e) J. Siminska-Stanny, M. Niziol, P. Szymczyk-Ziółkowska, M. Brozyna, A. Junka, A. Shavandi, D. Podstawczyk, *Addit. Manuf.* **2022**, 49; f) A.

Zolfagharian, S. Gharaie, A. Z. Kouzani, M. Lakhi, S. Ranjbar, M. L. Dezaki, M. Bodaghi, *Smart Mater. Struct.* **2022**, 31.

[14] C. Y. Lo, Y. S. Zhao, C. Kim, Y. Alsaid, R. Khodambashi, M. Peet, R. Fisher, H. Marvi, S. Berman, D. Aukes, X. M. He, *Mater. Today* **2021**, *50*, 35.

[15] a) H. H. Lu, B. Y. Wu, X. X. Yang, J. W. Zhang, Y. K. Jian, H. Z. Yan, D. C. Zhang, Q. J. Xue, T. Chen, *Small* **2020**, 16; b) P. Xue, C. Valenzuela, S. S. Ma, X. Zhang, J. Z. Ma, Y. H. Chen, X. H. Xu, L. Wang, *Adv. Funct. Mater.* **2023**, 33.

[16] a) D. Pan, D. Wu, P. J. Li, S. Y. Ji, X. Nie, S. Y. Fan, G. Y. Chen, C. C. Zhang, C. Xin, B. Xu, S. W. Zhu, Z. Cai, Y. L. Hu, J. W. Li, J. R. Chu, *Adv. Funct. Mater.* **2021**, *31*, 2009386; b) A. K. Mishra, T. J. Wallin, W. Y. Pan, P. Xu, K. Y. Wang, E. P. Giannelis, B. Mazzolai, R. F. Shepherd, *Sci. Robot.* **2020**, *5*, aaz3918; c) Y. S. Zhao, C. Y. Lo, L. C. Ruan, C. H. Pi, C. Kim, Y. Alsaid, I. Frenkel, R. Rico, T. C. Tsao, X. M. He, *Sci. Robot.* **2021**, *6*, eabd5483; d) L. X. Hu, P. L. Chee, S. Sugiarto, Y. Yu, C. Q. Shi, R. Yan, Z. Q. Yao, X. W. Shi, J. C. Zhi, D. Kai, H. D. Yu, W. Huang, *Adv. Mater.* **2023**, 35.

[17] a) M. T. Li, X. Wang, B. Dong, M. Sitti, *Nat. Commun.* **2020**, *11*, 3988;. b) L. Su, D. Jin, Y. Wang, Q. Wang, C. Pan, S. Jiang, H. Yang, Z. Yang, X. Wang, N. Xia, K. F. Chan, P. W. Y. Chiu, J. J.-Y. Sung, L. Zhang, *Sci. Adv.* **2023**, *9*, eadj0883.

[18] a) E. S. Keneth, A. Kamyshny, M. Totaro, L. Beccai, S. Magdassi, *Adv. Mater.* **2021**, *33*, 2003387; b) X. Kuang, D. J. Roach, J. T. Wu, C. M. Hamel, Z. Ding, T. J. Wang, M. L. Dunn, H. J. Qi, *Adv. Funct. Mater.* **2019**, *29*, 1805290; c) D. S. Wu, Y. N. Zhang, H. R. Yang, A. F. Wei, Y. X. Zhang, A. Mensah, R. Yin, P. F. Lv, Q. Feng, Q. F. Wei, *Mater. Horiz.* **2023**, *10*, 2587.

[19] a) R. S. Kularatne, H. Kim, J. M. Boothby, T. H. Ware, *J Polym. Sci. Pol. Phys.* **2017**, *55*, 395; b) H. S. Guo, A. Priimagi, H. Zeng, *Adv. Funct. Mater.* **2022**, 32; c) Y. H. Wu, S. Zhang, Y. Yang, Z. Li, Y. Wei, Y. Ji, *Sci. Adv.* **2022**, *8*; d) S. J. D. Lugger, L. Ceamanos, D. J. Mulder, C. Sanchez-Somolinos, A. P. H. J. Schenning, *Adv. Mater.* **2023**, *8*.

[20] a) Y. G. Guo, L. W. Liu, Y. J. Liu, J. S. Leng, *Adv. Intell. Syst.-Ger.* **2021**, *3*, 2000282; b) Q. G. He, Z. J. Wang, Y. Wang, A. Minori, M. T. Tolley, S. Q. Cai, *Sci. Adv.* **2019**, *5*, eaax5746; c) R. C. Lan, J. Sun, C. Shen, R. Huang, Z. P. Zhang, C. Ma, J. Y. Bao, L. Y. Zhang, L. Wang, D. K. Yang, H. Yang, *Adv. Funct. Mater.* **2020**, *30*, 2000252.

[21] a) M. Behl, A. Lendlein, *Soft Matter* **2007**, *3*, 58; b) L. Q. Ren, Q. Wu, Q. P. Liu, P. T. Hao, J. H. Tang, J. Y. Li, Y. L. He, K. Y. Wang, L. Ren, X. L. Zhou, B. Q. Li, H. L. Liu, *Mater. Des.* **2023**, 228; c) M. L. Dezaki, M. Bodaghi, *Sens. Actuators, A* **2023**, *349*.

[22] Y. Alapan, A. C. Karacakol, S. N. Guzelhan, I. Isik, M. Sitti, *Sci. Adv.* **2020**, *6*, abc6414.

[23] a) Y. K. Bai, J. W. Zhang, D. D. Wen, B. Yuan, P. W. Gong, J. M. Liu, X. Chen, *J. Mater. Chem. A* **2019**, *7*, 20723; b) X. Xie, X. Xu, Q. X. Zhu, S. R. Lu, Y. Q. Li, Y. K. Bai, *Mater. Chem. Front.* **2022**, *6*, 1973; c) Y. Q. Li, X. Xie, Q. X. Zhu, S. R. Lu, Y. K. Bai, *J. Mater. Chem. A* **2022**, *10*, 22205.

[24] a) J. W. Ambrose, N. Z. R. Chiang, D. S. Y. Cheah, C. H. Yeow, *Soft Rob.* **2023**, *10*, 301; b) D. Barpuzary, H. Ham, D. Park, K. Kim, M. J. Park, *ACS Appl. Mater. Interfaces* **2021**, *13*, 50381; c) L. Zhao, J. H. Huang, Y. C. Zhang, T. Wang, W. X. Sun, Z. Tong, *ACS Appl. Mater. Interfaces* **2017**, *9*, 11866; d) K. Luo, Q. Tian, H. Y. Hu, *Nonlinear Dynam.* **2020**, *102*, 1463.

[25] a) T. Ware, D. Simon, C. Liu, T. Musa, S. Vasudevan, A. Sloan, E. W. Keefer, R. L. Rennaker, W. Voit, *J. Biomed. Mater. Res.* **2014**, *102*, 1; b) S. M. Hosseini, R. Rihani, B. Batchelor, A. M. Stiller, J. J. Pancrazio, W. E. Voit, M. Ecker, *Front. Mater.* **2018**, 5.

[26] a) X. J. Zhou, L. H. Weng, Q. Chen, J. M. Zhang, D. Y. Shen, Z. C. Li, M. J. Shao, J. Xu, *Polym. Int.* **2003**, *52*, 1153; b) D. Kim, K. Park, *Polymer* **2004**, *45*, 189; c) E. Turan, T. Caykara, *J. Appl. Polym. Sci.* **2007**, *106*, 2000; d) G. Sennakesavan, M. Mostakhdemin, L. K. Dkhar, A. Seyfoddin, S. J. Fatihhi, *Polym. Degrad. Stabil.* **2020**, *180*, 109308.

[27] a) X. Kuang, J. T. Wu, K. J. Chen, Z. Zhao, Z. Ding, F. J. Y. Hu, D. N. Fang, H. J. Qi, *Sci. Adv.* **2019**, 5; b) G. I. Peterson, J. J. Schwartz, D. Zhang, B. M. Weiss, M. A. Ganter, D. W. Storti, A. J. Boydston, *ACS Appl. Mater. Interfaces* **2016**, *8*, 29037; c) X. R. Peng, L. Yue, S. Z. Liang, S. Montgomery, C. L. Lu, C. M. Cheng, R. Beyah, R. R. Zhao, H. J. Qi, *Adv. Funct. Mater.* **2022**, *32*, 2112329.

[28] a) G. Sennakesavan, M. Mostakhdemin, L. K. Dkhar, A. Seyfoddin, S. J. Fatihhi, *Polym. Degrad. Stabil.* **2020**, 180; b) H. J. Zhang, Y. R. Cheng, X. J. Hou, B. Yang, F. Guo, *New J. Chem.* **2018**, *42*, 9151.